A Numerical Study of Currents, Heat Advection, and Sea-Level Fluctuations in the Yellow Sea in Winter 1986

Y. HSUEH AND DONGLIANG YUAN

Department of Oceanography, The Florida State University, Tallahassee, Florida

(Manuscript received 30 October 1995, in final form 23 September 1996)

ABSTRACT

A vertically integrated model that incorporates horizontal temperature variations is used to study the circulation of the Yellow Sea in a wintertime period for which velocity and temperature measurements are available at several moorings locations along a central trough. The model features realistic bottom topography and is forced with wind stress and heat flux fields from 13 January to 22 February 1986. The model also incorporates, as a boundary condition, sea-level fluctuations derived from coastal and insular tide gauge stations along model boundaries in open waters.

The model reproduces well sea level fluctuations along the coasts of both China and Korea. The hindcast velocity time series, particularly for the north–south component, track those obtained from direct measurements at the moorings. The model momentum balance indicates that the northward flow in the trough is driven by a sea level setup to the south in response to northerly wind bursts in the winter monsoon. The sea-level fluctuations propagate around the Yellow Sea embayment in a counterclockwise sense and exhibit a northward increase in amplitude along both the China and Korea coasts, apparently due to the general shallowness of the northern reaches of the embayment. The lack of a suitable initial condition in temperature and the presence of large biases in the sea surface heat flux distribution preclude the hindcast of the temperature field. Yet trajectories of model fluid displacement confirm an overall northward transport of mass, and hence heat and salt, even though the northerly wind-pulse-dominated current fluctuates with a small mean.

While wintertime currents in the Yellow Sea appear dominated by the wind forcing, empirical orthogonal function analysis of model sea-level fluctuations attributes 48% of the variance to a mode whose time variation follows those of sea-level heights imposed along the open model boundaries. The mode with a time variation similar to that found in the wind stress magnitude time series accounts for only 28% of the variance. This suggests the domination of sea-level fluctuations by low-frequency fluctuations in the Kuroshio.

1. Introduction

The Yellow Sea is a north–south elongated, shallow embayment that lies between northern China and the Korean Peninsula (Fig. 1). The topography of the Yellow Sea features a central trough that opens to the Okinawa Trough southeast of Cheju, an area frequently reached by the Kuroshio. In fact, it has often been suggested that a branch of the Kuroshio intrudes landward along this central trough, bringing heat and salt into the northern reaches, hundreds of kilometers removed from the shelf break (Nitani 1972; Guan 1984). Direct observations of flow in this trough were not made, however, until the winter of 1986/87 when an array of moored current meters were deployed in the eastern Yellow Sea (Hsueh 1988) (see mooring locations in Fig. 1). The flow was found to be highly variable but well-correlated with northerly (southward) wind bursts associated with cold front passages, suggesting a wind-driven mechanism for its dynamics. Indeed, a long-wave theory that incorporates as a forcing function a wind stress calculated at a single point from geostrophic wind estimates has been able to account for this correlation (Hsueh and Pang 1989). Due to the idealization used, however, direct comparisons of time series between the calculation and observation were less than satisfactory. In particular, not discussed at all is the clear cooling trend observed in the temperature time series and the significance of the large horizontal temperature contrast observed in an infrared image of the Yellow Sea during the period of the mooring experiment (see Hsueh 1988). The purpose of the present study is thus to make such comparisons with the incorporation, in the calculation, of temperature contrasts during the mooring experiment and the realistic topography of the Yellow Sea.

To calculate the flow field, a vertically integrated, constant-density model of the Yellow Sea, previously used to study the sea level fluctuations, is adapted (Hsueh et al. 1986). It is tacitly assumed that in winter, vigorous wind stirring and convective overturning maintain the temperature, and hence density, uniform in the vertical (Lie 1985). The large temperature contrast in the horizontal must, how-

Corresponding author address: Prof. Y. Hsueh, Department of Oceanography, The Florida State University, Tallahassee, FL 32306-3048.
E-mail: hsueh@adin.ocean.fsu.edu

© 1997 American Meteorological Society

Unauthenticated | Downloaded 09/28/22 11:35 PM UTC

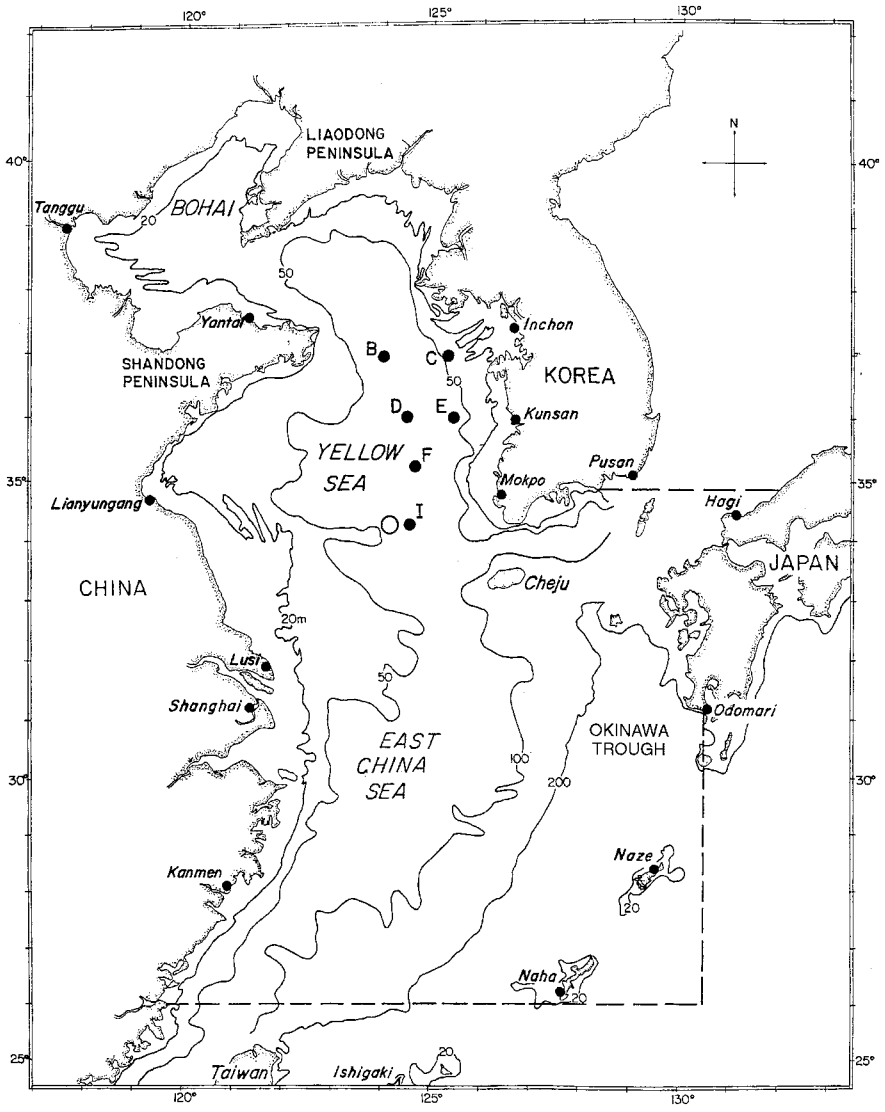

FIG. 1. Map of the marginal seas of northern China. Depths are in meters. Hourly sea–level heights at named tide gauge stations and bottom pressure measurements at mooring stations **B** and **D** for the period of 13 January through 23 February 1986 form the database for the sea level hindcast. Current velocity and temperature measurements at all the mooring stations, **B**, **D**, **F**, **I**, **C**, and **E**, provide the rest of the hindcast dataset. Open boundaries of the model are indicated with dashed straight lines. The open circle near mooring marks the position where time series of terms of the north–south momentum and heat equations are examined in detail.

ever, be incorporated. Thus adapted, the model is used to conduct a hindcast in which model time series are obtained for sea level fluctuations, current velocities, and temperature that may be compared with those observed at the moorings and coastal tide gauge stations. To the extent that the hindcast is successful, the model serves as a proxy for the study of the dynamics operative in the Yellow Sea, particularly the momentum and heat balances pertaining to the flow in the trough. In addition, the inclusion of the heat equation also allows an evaluation of the degree to which the wintertime temperature in the Yellow Sea may be predicted. In a companion study, an attempt is made to use the associated adjoint model to assimilate routinely reported sea surface temperatures so that a reasonably unbiased initial temperature condition and sea surface heat flux specification may be obtained for temperature forecasting (Yuan and Hsueh 1997, hereafter YH).

2. Model

The model geometry is exactly the same as in Hsueh et al. (1986) (see Fig. 1 for a demarcation of the model domain). The model equations remain similar except that a vertically integrated heat equation is included,

Unauthenticated | Downloaded 09/28/22 11:35 PM UTC

friction is quadratic in vertically averaged velocities, and a buoyancy term is present in the momentum equation (Yuan 1995). It is tacitly assumed that, most of the time, wind stirring and convective overturning prevent re-stratification and that even for low-wind speed conditions, the slope of isotherms away from the vertical is small so that vertical homogeneity remains a good approximation. Keeping the same notation as before, the governing equations are thus

$$\frac{\partial U}{\partial t} - 2\Omega \sin\varphi V = -gh\frac{\partial \zeta}{\partial x} + \frac{1}{2}g\alpha h^2\frac{\partial T}{\partial x} + \frac{\tau^x}{\rho m} - \frac{r}{\rho m h^2}U(U^2+V^2)^{1/2}, \quad (1)$$

$$\frac{\partial V}{\partial t} + 2\Omega \sin\varphi U = -gh\frac{\partial \zeta}{\partial y} + \frac{1}{2}g\alpha h^2\frac{\partial T}{\partial y} + \frac{\tau^y}{\rho m} - \frac{r}{\rho m h^2}V(U^2+V^2)^{1/2}, \quad (2)$$

$$\frac{\partial \zeta}{\partial t} + m^2\left(\frac{\partial U}{\partial x} + \frac{\partial V}{\partial y}\right) = 0, \quad (3)$$

$$\frac{\partial hT}{\partial t} + m^2\frac{\partial UT}{\partial x} + m^2\frac{\partial VT}{\partial y} = m^2K_H\left[\frac{\partial}{\partial x}\left(h\frac{\partial T}{\partial x}\right) + \frac{\partial}{\partial y}\left(h\frac{\partial T}{\partial y}\right)\right] - \frac{Q}{\rho c_p}, \quad (4)$$

where m is the Mercator map scale given for a projection latitude, $\varphi_1 = 33°$, by

$$m = \frac{\cos\varphi_1}{\cos\varphi}, \quad (5)$$

(U, V) are (x, y) components of the volume transport divided by m, and (τ^x, τ^y) are wind stress components; Q is the sea surface heat flux, positive when it is from the ocean to the atmosphere; $T = T(x, y)$ is temperature; α is the thermal expansion coefficient, set equal to 10^{-4} °C^{-1}; c_p the specific heat; and $K_H = 10^6$ cm^2 s^{-1}, the horizontal eddy diffusivity; $\Omega = 7.292 \times 10^{-5}$ s^{-1} is the earth's rotation speed; φ the latitude; g the gravity; $h = h(x, y)$ the water depth; ζ the sea level elevation perturbation from the mean sea level; and ρ the seawater density that is set to be 1.0 g cm^{-3}. The quadratic frictional coefficient r is set to 2.722×10^{-3}, corresponding to a Chezy coefficient to 60 m$^{1/2}$ s^{-1} (see, e.g., Chow 1959).

The time window for which (1)–(4) are integrated spans forty days, 0000 JLT (Japan Local Time) 13 January to 0000 JLT 22 February 1986. This time window is the period during which the northerly wind bursts are the most vigorous (Hsueh 1988). The wind stress is calculated every 6 hours from geostrophic wind velocities, exactly as in Hsueh et al. (1986). For the sea surface heat flux Q, values on the model grid calculated in a previous heat budget study are used (Hsueh and Tinsman 1991). The model is also driven by 40-h low-pass filtered sea level variations along open boundaries at 26°N, 130°20′E and 34°48′N in the Tsushima Strait. These variations are obtained from records at coastal and insular tide gauge stations and are imposed as a 92-day mean sea level slope plus a deviation therefrom, in a similar manner as in Hsueh et al. (1986). The mean slope, in the present case, translates into a Kuroshio inflow of 31 Sv (Sv $\equiv 10^6$ m^3 s^{-1}) through the southern boundary in the longitudinal span between Ishigaki and Naha, an outflow of 3 Sv through Tsushima Strait between Pusan and Hagi, and a Kuroshio outflow of 28 Sv through Tokara Strait on the eastern open boundary south of Odomari.

The model is started from a state of rest. The initial temperature distribution is characterized by straight isotherms oriented southwest to northeast, starting with 20°C in the southeast corner to 1°C to the extreme northwest. This hypothetical distribution captures the observed general gradient of the isotherms and the winter temperature contrast in the Yellow Sea, but provides no guarantee that the model temperatures would agree, in the absolute sense, with temperatures observed at the moorings. Even assuming that the sea surface heat flux and heat advection are correctly calculated, the most that could be hoped for is, perhaps, agreement in the cooling trend as the model proceeds forward in time.

In the computational lattice, the temperature is placed at the ζ-point and the integration of the momentum and continuity equations proceeds in two half time steps (see Hsueh et al. 1986). The temperature is computed after the velocity, so the buoyancy term lags one full time step. The no-normal heat flux condition is enforced on physical boundaries. On open boundaries, the radiation condition is applied. In mathematical terms, in case of an outflow,

$$T^{N+1} = T^N - \Delta t\left(\frac{V_n}{H}\frac{\partial T}{\partial n}\bigg|^N + \frac{Q^N}{\rho c_p}\right),$$

where V_n is the component of calculated transport perpendicular to the open boundary, positive when outward, and n, the outward-normal distance to the open boundary, and the superscript denotes the time level.

In case of an inflow,

$$T^{N+1} = T^N - \frac{Q^N\Delta t}{\rho c_p}.$$

3. Results

a. Sea-level fluctuations

Output from the 40-day model run consists of grid-point sea level fluctuations, volume transports, and tem-

Unauthenticated | Downloaded 09/28/22 11:35 PM UTC

peratures. The calculated sea level at a grid point in the neighborhood of a tide gauge station is compared to the observation made at that station. For stations on the coast of Korea, (Fig. 2) comparisons are made at Inchon, Kunsan, and Mokpo along the west coast of Korea and at mooring stations in the trough at B and D, where bottom pressure measurements are available (Hsueh 1988). The model-generated time series track well those observed at all stations, notably better than that achieved analytically in Hsueh and Pang (1989). The result is, however, qualitatively similar to that achieved with the 1980/81 winter hindcast in which the horizontal temperature contrast was not imposed (Hsueh et al. 1986). The coherence and phase calculation for each pair of model and observation time series confirms this visual impression (Fig. 3).

The comparison along the coast of China is similarly successful. Figure 4 shows the comparison at Tanggu, at the western edge of Bohai; Yantai, at the southern coast of the strait between Liaodong Peninsula and Shandong Peninsula; Lianyungang, a coastal station 200 km shoreward from the 50-m isobath; and Lusi and Kanmen, along the coastline to the south. The coherence and phase calculation underscores the similarity of the time series (Fig. 5). In fact, the coherency at the low-frequency end remains high except for Yantai, indicating a better overall agreement than that on the coast of Korea. A visual inspection confirms this.

The highs and lows in the sea-level curves also seem to align themselves along straight lines across the time series, indicating a phase propagation. The arrival of events appears later in time from Tanggu to Kanmen on the coast of China. The indication is less clear on the coast of Korea because the stations span a relatively short alongshore distance. Yet, a small lag in the arrival time can be detected from Mokpo to Inchon. Propagating Kelvin waves that move northward along the Korean west coast have been shown to be a part of the sea-level response in the wintertime Yellow Sea (Hsueh and Romea 1983). The coherence and phase calculation for both model and observed sea-level time series at Tanggu and Lianyungung, for example, produce a 72° lead in phase by sea-level fluctuations at Tanggu at the frequency of 0.4 cpd where the coherence is nearly one. This lead translates into a southward phase propagation along the China coast at a speed on the order of several meters per second. Similar calculations for the sea-level time series at Tanggu and Kanmen farther to the south yields similar results. With the propagation along the coast of China now confirmed, it appears that the sea-level response in the Yellow Sea in wintertime is organized into a rotary wave that propagates around the Yellow Sea in a counterclockwise direction, as suggested in Hsueh et al. (1986).

In addition, a northward increase in amplitude of sea level fluctuations occurs along the coasts of both China and Korea (see Figs. 2 and 4). While the termination of the coastline at the end of a peninsula argues for the existence of a node in sea-level fluctuations near Mokpo, providing a reason for the increase on the coast of Korea, no such explanation is available for the increase on the coast of China (Clarke and Van Gorder 1986; Hsueh and Pang 1989). A mechanism that works to produce an increase on both coasts is the approximate constancy of meridional energy flux of Kelvin waves, which have been shown to carry most of the coastal sea-level variance (Hsueh and Pang 1989). For the straight coastline case of a Kelvin wave in water of a constant depth, h_0, the mean alongshore energy flux is (see Gill 1982)

$$\frac{1}{4}\frac{\rho g^2 h_0 \zeta_0^2}{|f|},$$

where ζ_0 is the Kelvin wave amplitude in sea-level height.

Thus, the amplitude of such a Kelvin wave increases as the wave travels into a region of shallow water and high latitude and decreases as it moves away from such a region. The increase in amplitude of sea level fluctuations along the coasts of both China and Korea is probably a consequence of the fact that the Yellow Sea covers a large latitudinal stretch and shoals to the north.

b. Velocities

Current velocities at the grid points near the moorings are obtained from volume transports divided by the local water depth. Figure 6 shows the comparison between the north–south current velocities from the model and observations made at mid depth at moorings B, D, F, and I in the trough and at 1 m above the bottom at moorings C and E near the 50-m isobath on the eastern flank. There is again an improvement over that achieved in Hsueh and Pang (1986) in terms of the agreement at B, D, F, and I. [There were no current observations, and therefore, no current comparisons for the 1980/81 hindcast (Hsueh et al. 1986)]. The failure of the model in reproducing the observations at C and E is, however, similar to that in Hsueh and Pang (1986). The coherence and phase calculation supports these impressions (Fig. 7).

The east–west velocities again prove the least reproducible, even with alongshore variations now incorporated to the extent possible with the model resolution (see Hsueh and Pang 1986). Figure 8 shows the comparison between the model output and the observations at all mooring stations. Only at F and I does one see some agreement. Hsueh and Pang (1986) exhibits similar agreement at F, but produces no useful comparison at I. It appears that the cross-shore velocity calculation is sensitive to alongshore variations on scales perhaps less than those that can be resolved in the present model, in terms both of grid spacing (31.15 km) and wind stress distribution (see Brink et al. 1987). The coherence and phase calculation show some deterioration from those for the north–south components (Fig. 9), although the calculations at B, I, C, and E remain similar at periods greater than 2 days.

Unauthenticated | Downloaded 09/28/22 11:35 PM UTC

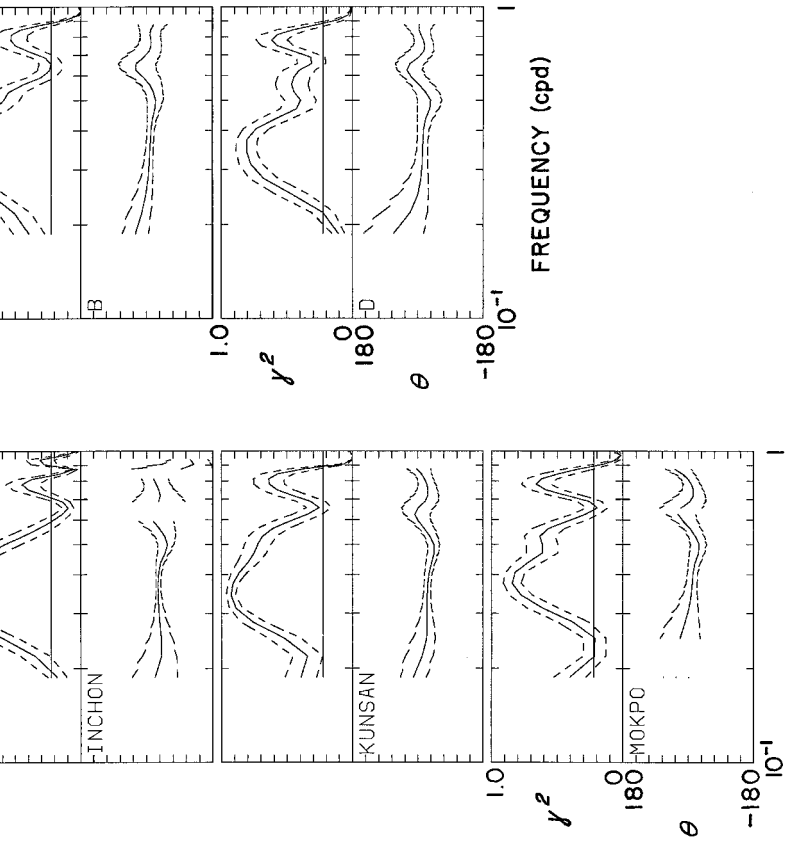

FIG. 3. Coherency squared, γ^2, and phase, θ, between the observed and hindcast sea-level fluctuations presented in Fig. 2, plotted station by station in separate panels with the same abscissa and ordinate. The solid horizontal line in the coherency plot indicates the 95% confidence level and the dashed curves mark the 99.5% confidence interval of the calculation.

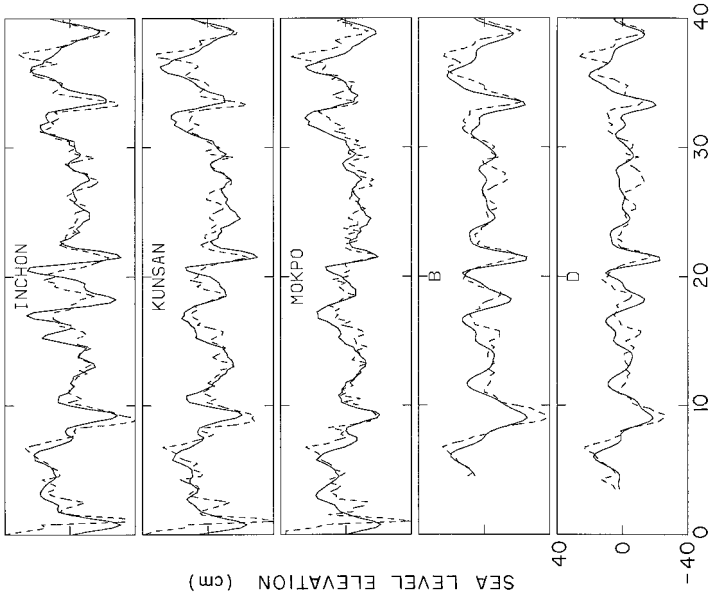

FIG. 2. Comparison between observed and hindcast sea level heights at locations along the Korea coast and at mooring stations **B** and **D** for the 40-day period for which the hindcast is conducted. Observed values (solid curve) have been low-pass filtered and adjusted for the atmospheric pressure, and both the observed and calculated sea level heights are demeaned. The abscissa and ordinate are as given in the bottom panel.

Unauthenticated | Downloaded 09/28/22 11:35 PM UTC

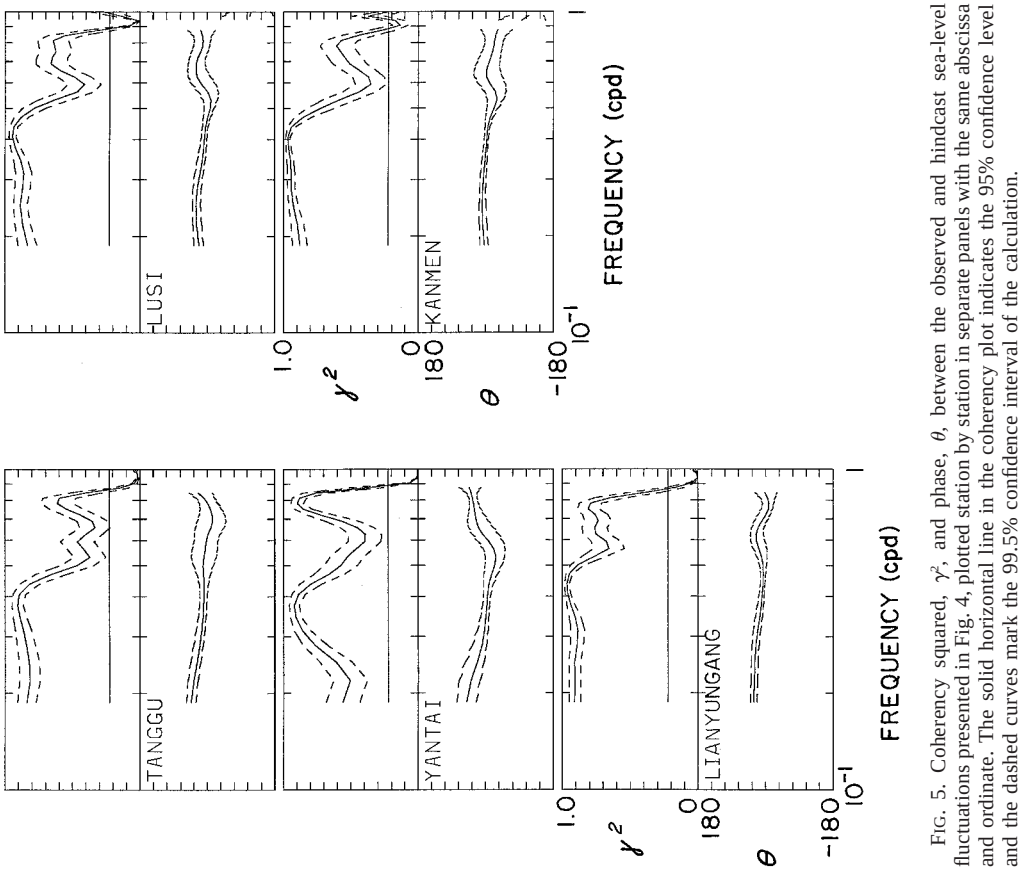

FIG. 5. Coherency squared, γ^2, and phase, θ, between the observed and hindcast sea-level fluctuations presented in Fig. 4, plotted station by station in separate panels with the same abscissa and ordinate. The solid horizontal line in the coherency plot indicates the 95% confidence level and the dashed curves mark the 99.5% confidence interval of the calculation.

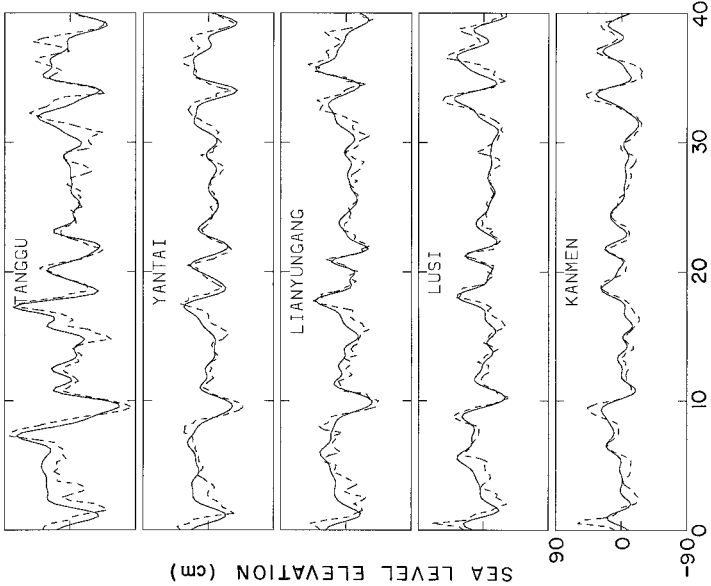

FIG. 4. Comparison between observed and hindcast sea-level heights at locations along the China coast for the 40-day period for which the hindcast is conducted. Observed values (solid curve) have been low-pass filtered and adjusted for the atmospheric pressure and both the observed and calculated sea-level heights are demeaned. The abscissa and ordinate are as given in the bottom panel.

Unauthenticated | Downloaded 09/28/22 11:35 PM UTC

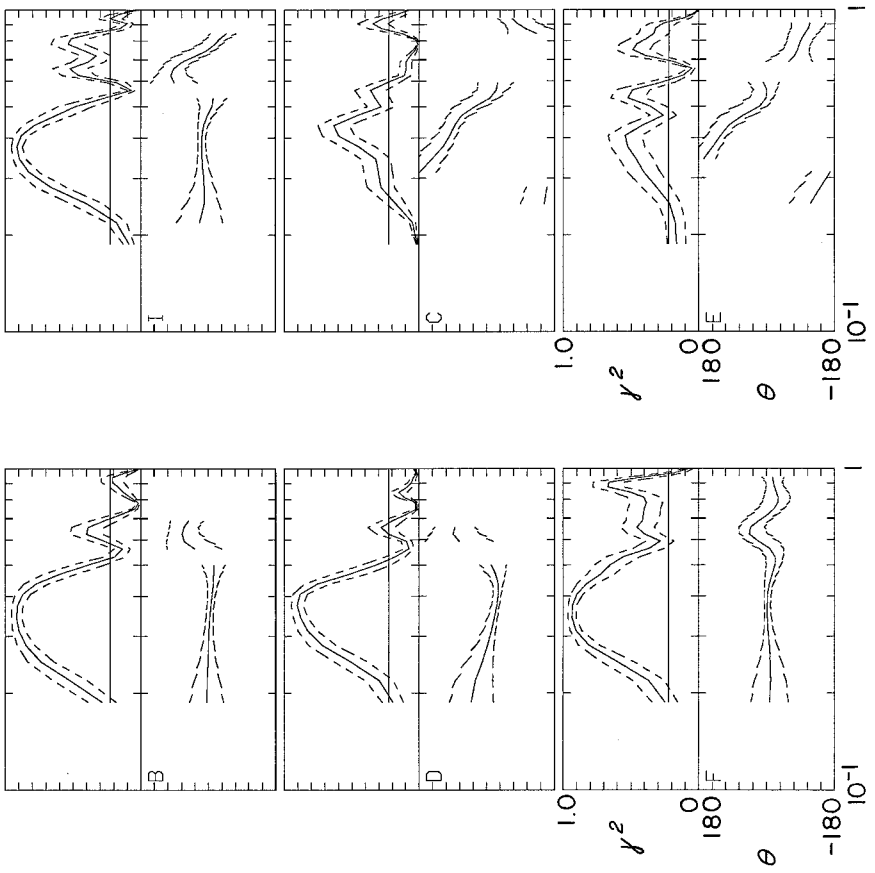

FIG. 7. Coherency squared, γ^2, and phase, θ, between the observed and hindcast velocity fluctuations presented in Fig. 6, plotted station by station in separate panels with the same abscissa and ordinate. The solid horizontal line in the coherency plot indicates the 95% confidence level and the dashed curves mark the 99.5% confidence interval of the calculation.

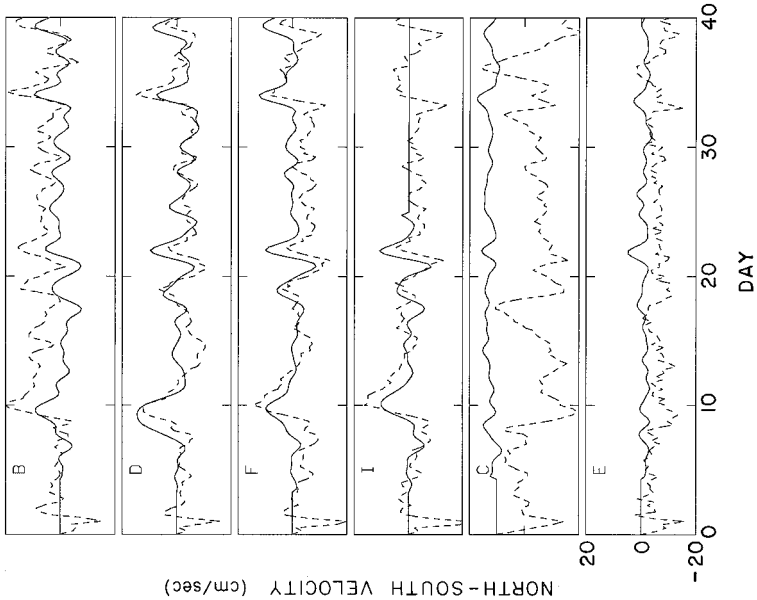

FIG. 6. Comparison between observed and hindcast north–south velocity in the Yellow Sea trough for the 40-day period for which the hindcast is conducted. Observed values (solid curve) are low-pass filtered. Time span over which there is no observation is covered with solid horizontal lines. The abscissa and ordinate are as given in the bottom panel.

Unauthenticated | Downloaded 09/28/22 11:35 PM UTC

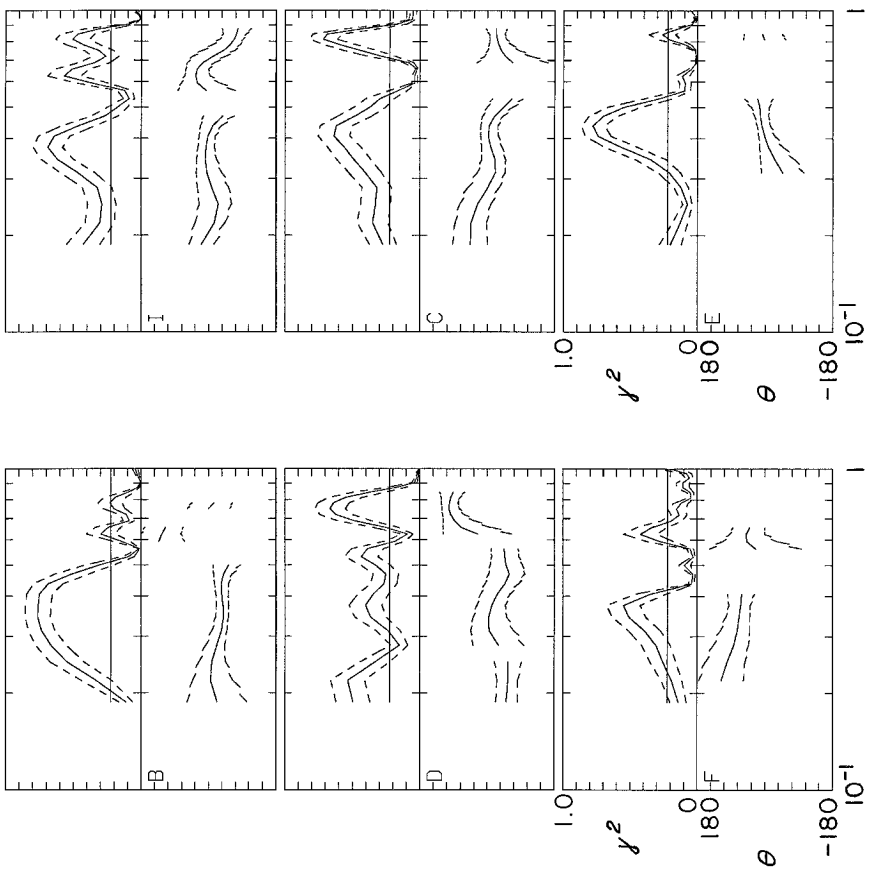

FIG. 9. Coherency squared, γ^2, and phase, θ, between the observed and hindcast velocity fluctuations presented in Fig. 8, plotted station by station in separate panels with the same abscissa and ordinate. The solid horizontal line in the coherency plot indicates the 95% confidence level and the dashed curves mark the 99.5% confidence interval of the calculation.

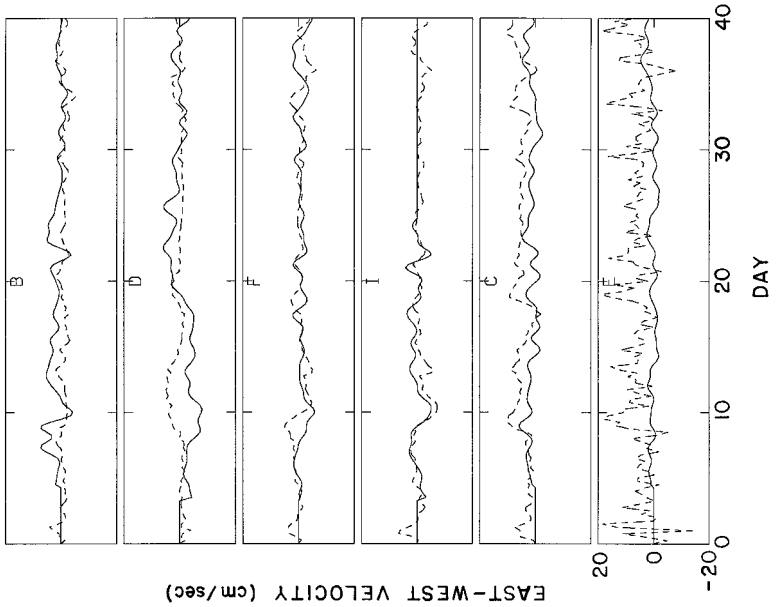

FIG. 8. Comparison between observed and hindcast east–west velocity in the Yellow Sea trough for the 40-day period for which the hindcast is conducted. Observed values (solid curve) are low-pass filtered. Time span over which there is no observation is covered with solid horizontal lines. The abscissa and ordinate are as given in the bottom panel.

Unauthenticated | Downloaded 09/28/22 11:35 PM UTC

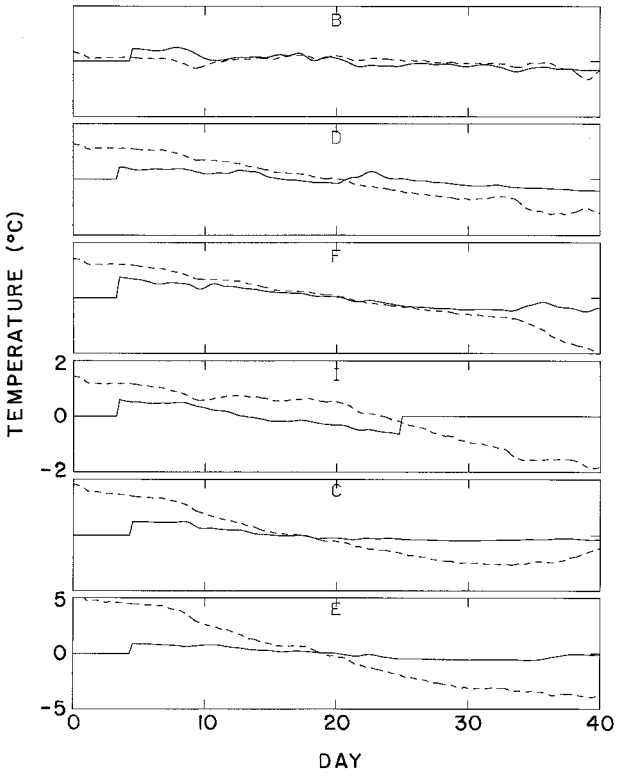

FIG. 10. Comparison between observed and hindcast temperature in the Yellow Sea trough for the 40-day period for which the hindcast is conducted. Observed values (solid curve) are low-pass filtered. Both the observed and calculated temperatures are demeaned. Time span over which there is no observation is covered with solid horizontal lines. Note that plots for **C** and **E** share the same ordinate and plots for **B**, **D**, **F**, and **I** share the other.

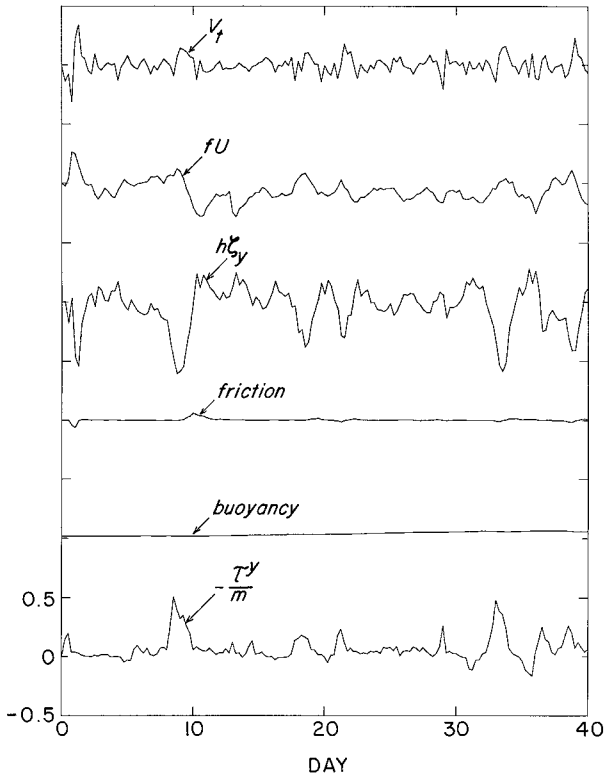

FIG. 11. Time series of terms of the nondimensionalized (2) at a grid point whose position is indicated with the open circle in Fig. 1. At any given time, the ordinates add to zero. To obtain dimensional values in cgs units, multiply each by the factor of 4.584. The curves share the same ordinate and abscissa.

c. Temperature

As expected, the calculated temperatures differ from those observed in the mean to the extent that the initial condition has not been adequately specified. The difference varies but is on the order of 1°C. Thus, only the comparison of the demeaned temperature is presented. Based on the comparison at all the mooring stations (Fig. 10), other than at B, the model overestimates the mean rate of cooling, more so at C and E. The coherence and phase calculation (not shown) adds little more. The cooling rate at a given point in the Yellow Sea in winter depends upon the rate at which heat is advected and the rate at which it is lost to the atmosphere (see later in dynamic balances). The good agreement in current velocity, therefore in heat advection, in the trough probably explains the relatively successful comparison in the cooling rate there. The remaining discrepancy is probably rooted in the error in the specification of the sea surface heat flux Q. Using a variational data assimilation procedure together with the present model, YH have successfully reduced the errors in both Q and the initial temperature condition and made significant improvement in reproducing the cooling trend in the trough.

d. Dynamic balances

Since as the model appears to produce sea-level and flow responses closely resembling those observed, the model dynamics may be studied to gain an insight into the physical processes that are locally operative in the Yellow Sea. The time series of terms of (2) at a grid point in the trough near mooring station I (18, 31) (see Fig. 1 for the position) are examined (Fig. 11). All the terms are nondimensionalized and transposed to the left so that the sum of the ordinates is zero. Since the model coast in the neighborhood of this grid point is oriented north–south, (2) is here equivalent to a statement of alongshore momentum balance. (The alongshore flow is nearly perfectly balanced with the cross-shore sea level gradient.) The dominance of the sea-level setup to the south in response to peaks in the northerly wind is apparent. In each case, an acceleration of the flow toward the north follows immediately, suggesting that in the Yellow Sea in wintertime the flow in the trough indeed arises as a compensation for the southward wind-driven coastal current. In addition, both the friction and

Unauthenticated | Downloaded 09/28/22 11:35 PM UTC

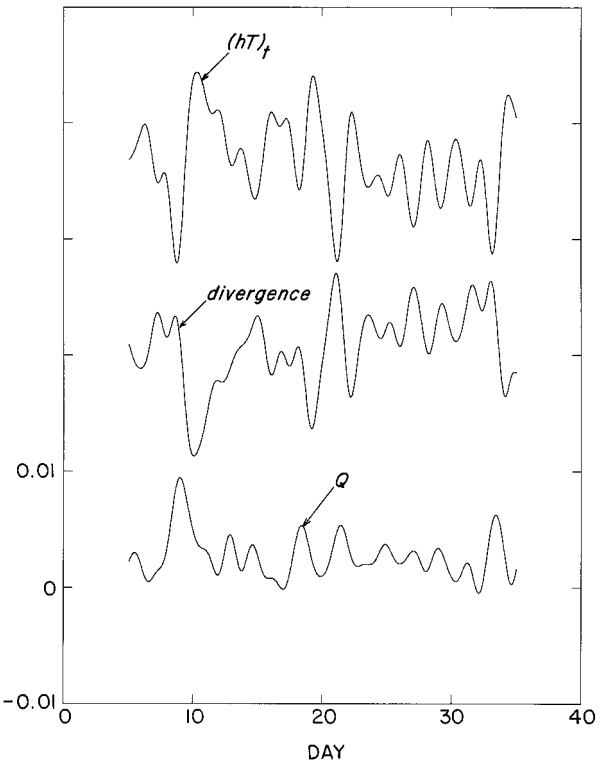

FIG. 12. Time series of terms of the nondimensionalized (4) at a grid point whose position is indicated with the open circle in Fig. 1. To obtain dimensional values (in units of cm °C day^{-1}), multiply each by the factor 0.188×10^5. The curves share the same ordinate and abscissa.

buoyancy terms are clearly negligible. Figure 11 is essentially the same as Fig. 15 in Hsueh et al. (1986). The similarity implies that the horizontal temperature contrast is of little importance in the dynamical sense. The smallness of the buoyancy term is nevertheless significant because it allows the momentum equation to be decoupled from the heat equation, an important point for the inverse calculation of Q in YH. The smallness of the friction term explains the slight time lag of the local acceleration due to the wind stress in the momentum balance and lends credence to the argument of energy flux constancy used before in the explanation of the northward increase of sea-level amplitudes.

Figure 12 presents the time series at the same grid point of terms of the heat equation, (4), nondimensionalized. The advective terms are combined into one divergence term, and the diffusion terms are negligibly small and are not shown. The terms are low-pass filtered to eliminate the component arising from the diurnal heating cycle. The fluctuations in the local time variation and the divergence terms are of the same order of magnitude, but those in the sea surface heat flux term are notably smaller. However, short-duration fluctuations in the local time variation amount to minor temperature changes of the order of 0.1°C (Fig. 10). The long-term cooling trend, which is so prominent in Fig. 10, actually depends on the balance in the mean, which happens to be mainly between the sea surface heat flux (2.52×10^{-3}) and the local derivative (-3.27×10^{-3}). Thus, in hindcasting the long-term cooling trend, a reliable estimate of Q is still the key factor (see YH). (The mean value of the divergence term is 8.4×10^{-4}.)

On a several-day timescale, the balance is clearly between the local time change and divergence. The advective terms are each individually larger than the divergence term by a factor of ~5; thus, they tend to cancel. The reason for this is that in the Yellow Sea in wintertime, the temperature distribution is very nearly a function of water depth (see, e.g., Guan 1984). Together with the fact that the horizontal flow is nearly nondivergent, the divergence term in (4) must be small. Except for the first few days when the temperature is dominated by the initial condition, the model temperature field (not shown) controlled by the northward flow in the trough is indeed quite similar to the water depth field. Thus, the two advective terms in (4) tend to cancel, and the fluctuation in the divergence term actually arises as a residual. The success of the temperature hindcast on a several-day timescale is thus predicated upon an accurate calculation of the velocity, both cross-shore and alongshore. The poor performance of the model in terms of the temperature hindcast is thus attributable in part to the failure of the model to calculate the cross-shore velocity accurately.

e. Empirical orthogonal function analysis

In order to gain an understanding of the overall response patterns of the wintertime Yellow Sea to momentum inputs, an empirical orthogonal function analysis is conducted with the model outputs of sea-level fluctuations and velocities.

1) SEA-LEVEL FLUCTUATIONS

From the eigenfunction and time series of the first two sea level modes, the first mode (Fig. 13a) accounts for nearly 47% of the variance of the model sea-level fluctuation. Its time series tracks well the normalized low-pass filtered sea-level fluctuations at Naze (Fig. 13b). In fact, similar time series comparisons result for any of the tide gauge stations on the model open boundary, indicating perhaps that the first mode is driven by sea-level fluctuations associated with the Kuroshio. The northward increase in amplitude of the first mode reflects perhaps the amplification referred to in section 3a. The second mode (Fig. 13c) with a sea-level rise along the coast of China accounts for 30% of the variance and appears driven by the first-mode wind stress distribution (not shown, but accounting for 70% of the variance), which is nearly uniformly southward. The similarity in appearance between the time series of the second mode and that of the first-mode wind stress magnitude confirms this contention (Fig. 13d). The pattern of the sec-

Unauthenticated | Downloaded 09/28/22 11:35 PM UTC

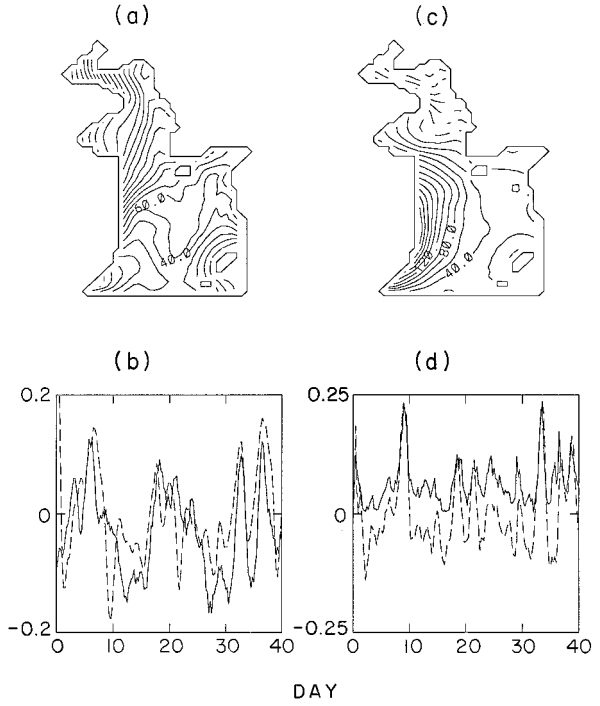

FIG. 13. Results from EOF analysis of hindcast sea-level fluctuations. (a) The first EOF mode contoured at intervals of 10, which accounts for 46.92% of the variance. (b) Comparison of the time function of the first EOF mode (dashed curve) with the standardized observed sea-level fluctuations at Naze (solid curve) (see Fig. 1 for location). (c) The second EOF mode contoured at intervals of 20, which accounts for 30.17% of the variance. (d) Comparison of the time function of the second EOF mode (dashed curve) with the time function of the magnitude of the first wind stress EOF mode (solid curve). The first wind stress EOF mode accounts for more than 70% of the wind stress variance.

ond-mode eigenfunction also is consistent with the spatial distribution of surface winds in wintertime that features a strong wind from the north, particularly along the coast of China.

2) CURRENT FLUCTUATIONS

From the results of the vector EOF analysis of the demeaned current velocity field the first mode (Fig. 14a), which accounts for 36% of the variance, has a spatial distribution very similar to that of the first EOF mode of the wind stress (not shown). The first-mode time function bears a resemblance to that of the wind stress in that agreement in argument occurs at the same time as agreement in normalized magnitude (Fig. 14b). The second mode shares the same comparison characteristics, but to a lesser extent (Figs. 14c and 14d). This similarity persists until the fifth mode, suggesting that the current fluctuations are primarily wind driven. Since the mean current is very nearly zero, judging from the north–south velocity plots (see Fig. 6), this implies that the currents themselves are primarily wind driven.

f. Particle trajectories

As mentioned in the introduction, an infrared image of sea surface temperature of the Yellow Sea shows a large horizontal contrast during the period of the mooring experiment (Hsueh 1988). The image features a patch of anomalously high temperature in the trough in contrast to low temperature strips along the coasts of both China and Korea. To the extent that the diffusion of heat is small, this anomaly pattern must be explicable in terms of advective transport. (It must be cautioned, however, that the horizontal temperature contrast in the pattern itself may be due in part to the difference in depth.) Particle trajectories calculated from the model velocity field with the Runge–Kutta method (Fig. 15) indicate that the modeled advective transport is indeed consistent with such observed surface features. Hypothetical particles are tracked from starting points along four zonal sections, at 33°00′, 34°20′, 35°40′, and 37°00′N. The particles are tracked from 23 January to 21 February. The net northward displacement is clearly shown in the trough, in contrast to along the coastal strip of Korea where the net displacement is southward and large. Along the coast of China the movement is mixed, resulting in small displacements. This circulation of particles must be accompanied by a transport of heat, giving rise to a water warming in the trough and cooling in the coastal strips. As a consequence, a warm tongue centered on the trough characterizes the temperature distribution. The trajectories even outline the orientation of the tongue very similar to that shown in the infrared image (see Hsueh 1988). Thus, the warm tongue represents advection by a wind-driven trough flow, not a branch of the Kuroshio, as previously concluded (Nitani 1972; Guan 1984).

4. Conclusions

A hindcast was conducted of sea-level height, current velocity, and temperature in the Yellow Sea in winter 1986, during an interval when continuous current meter measurements were available from a mooring array in the eastern Yellow Sea. The hindcast was based upon a vertically integrated numerical model that incorporates realistic bottom topography and a horizontal temperature contrast typically found in winter. The model was driven with wind stress and sea surface heat flux fields constructed for the hindcast period from routinely published surface pressure charts, atmospheric variables observed at coastal locations, and ship reports of sea surface temperature.

The hindcast has been particularly successful in reproducing sea level heights along the coasts of both Korea and China and north–south velocity in the central trough. The balance of modeled momentum in the north–south direction establishes that northward current surges in the trough are driven by sea level setup

Unauthenticated | Downloaded 09/28/22 11:35 PM UTC

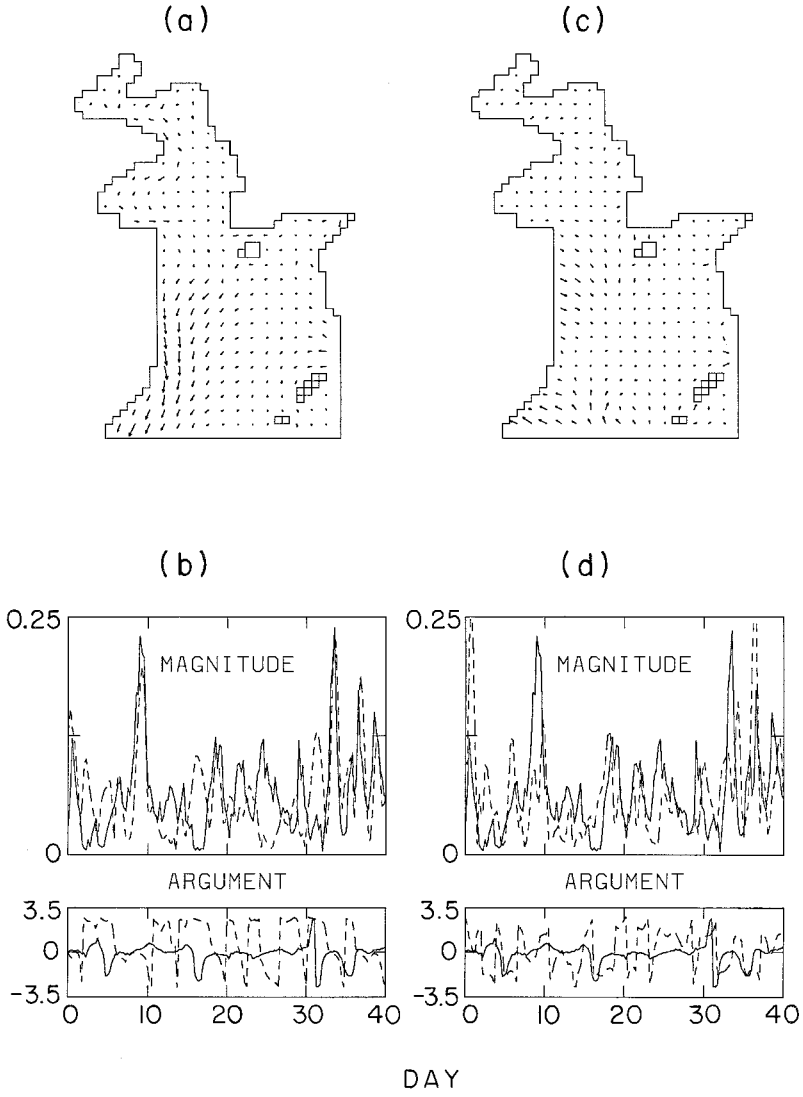

FIG. 14. Results from vector EOF analysis of hindcast velocity fluctuations. (a) Vector plot of the first EOF mode, which accounts for 36.14% of the variance. (b) Comparison of magnitude and phase between the first EOF mode (dashed curve) and the first wind stress EOF mode (solid curve). (c) Vector plot of the second EOF mode, which accounts for 30.17% of the EOF mode (dashed curve) and the first wind stress EOF mode (solid curve). The first wind stress EOF mode accounts for more than 70% of the wind stress variance.

in response to northerly wind pulses during the winter monsoon. The sea-level fluctuations are organized in a rotary wave that sweeps the Yellow Sea in a counterclockwise direction. The fluctuation amplitude increases to the north, probably due to the fact that the Yellow Sea shoals to the north and that friction is nearly negligible. While the current fluctuations appear dominated by local wind forcing, the sea-level fluctuations seem primarily a response to low-frequency fluctuations in the Kuroshio imposed remotely at the model open boundaries. The model/observation comparison in sea-level heights is qualitatively similar to that in an earlier effort when the thermodynamics were completely ignored (Hsueh et al. 1986), suggesting that the incorporation of the large horizontal temperature contrast is unimportant dynamically. The incorporation of realistic bottom topography is probably essential, particularly for the simulation of the observed velocity field, which was not available in the earlier effort.

The lack of a suitable initial temperature condition and the presense of errors in the sea surface heat flux distribution contribute to a temperature hindcast that is less than satisfactory. The balance of terms in the heat equation indicates that the calculation of short-duration fluctuations in the local time change of tem-

Unauthenticated | Downloaded 09/28/22 11:35 PM UTC

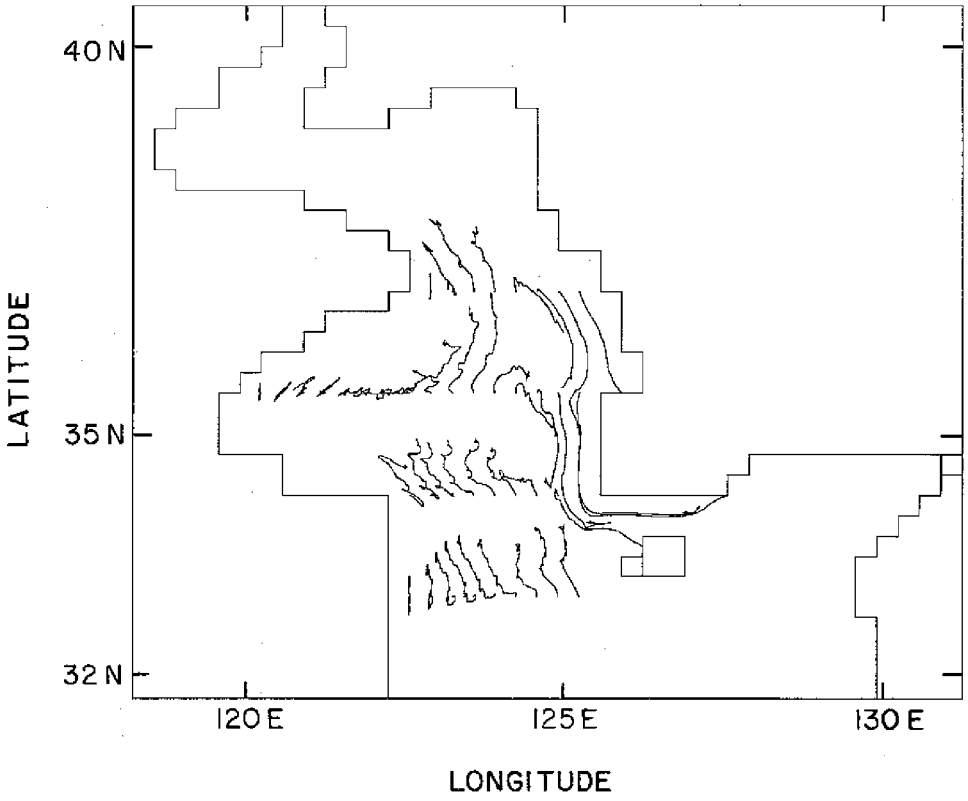

FIG. 15. Simulated particle trajectories in the Yellow Sea from 23 January to 21 February 1986. The particles are tracked from model grid points along four zonal sections, at 33°00′N, 34°20′N, 35°40′N, and 37°00′N.

perature is sensitive to advection, rendering the hindcast of temperature changes difficult on a several-day timescale. On the long-term, the balance in the mean shifts such that the sea surface heat flux overwhelms advection, suggesting that perhaps the hindcast on a longer timescale, such as a season, may be fruitful with an optimized sea surface heat flux field.

Although the currents in the central trough are episodic with a near zero mean, particle trajectories calculated from the model flow field exhibit a net northward displacement, indicating a transfer of heat northward. These trajectories are consistent with the tongue-like distribution of high temperature anomalies centered along the trough, as seen in an infrared image of the sea surface.

Acknowledgments. The reported research is supported by the National Science Foundation Grants OCE-9115365 and OCE95-29289, by the Coastal Sciences Program of the Office of Naval Research Grant N00014-90-J-1820, by the Physical Oceanography Program of the Office of Naval Research Grant N00014-95-1-0501, and by the Minerals Management Service Cooperative Agreement No. 14-35-0001-30804. The second author wishes to express his gratitude to Li Wenhai and Wang Ji of the National Marine Environmental Data and Information Service of China for providing the China coastal sea level data. He also wishes to thank Mr. Takashi Yoshida of the Oceanographical Division of the Japan Meteorological Agency for providing the ten-day mean sea surface temperature data.

REFERENCES

Brink, K. H., D. C. Chapman, and G. R. Halliwell Jr., 1987: A stochastic model for wind-driven currents over the continental shelf. *J. Geophys. Res.*, **92,** 1783–1797.

Chow, V. T., 1959: *Open-Channel Hydraulics.* McGraw-Hill, 680 pp.

Clarke, A., and S. Van Gorder, 1986: A method for estimating wind-driven frictional, time-dependent stratified shelf and slope water flow. *J. Phys. Oceanogr.*, **16,** 1013–1028.

Gill, A. E., 1982: *Atmosphere-Ocean Dynamics.* Academic Press, 662 pp.

Guan, B., 1984: Major features of the shallow water hydrography in the East China Sea and Huanghai Sea. *Ocean Hydrodynamics of the Japan and East China Sea,* T. Ichiye, Ed., Elsevier Oceanogr. Ser., Vol. 39, Elsevier, 1–13.

Hsueh, Y., 1988: Recent current observations in the eastern Yellow Sea. *J. Geophys. Res.*, **93,** 6875–6884.

——, and R. D. Romea, 1983: Wintertime winds and coastal sea-level fluctuations in the northeast China Sea. Part I: Observations. *J. Phys. Oceanogr.*, **13,** 2091–2106.

——, and I.-C. Pang, 1989: Coastal trapped long waves in the Yellow Sea. *J. Phys. Oceanogr.*, **19,** 612–625.

——, and J. H. Tinsman, 1991: Synoptic band wintertime heat ex-

Unauthenticated | Downloaded 09/28/22 11:35 PM UTC

change in the Yellow Sea. *Oceanography of Asian Marginal Seas,* K. Takano, Ed., Elsevier Oceanogr. Ser. Vol. 54, 269–276.

——, R. D. Romea, and P. W. deWitt, 1986: Wintertime winds and sea-level fluctuations in the northeast China Sea. Part II: Numerical model. *J. Phys. Oceanogr.,* **16,** 241–261.

Lie, H.-J., 1985: Wintertime temperature-salinity characteristics in the southern Hwanghae (Yellow Sea). *J. Oceanogr. Soc. Japan,* **41,** 291–298.

Nitani, T., 1972: Beginning of the Kuroshio. *Kuroshio, Physical Aspect of the Japan Current,* H. Stommel and K. Yoshida, Eds., University of Washington Press, 129–156.

Yuan, D., 1995: Toward the prediction of surface temperature in the Yellow Sea in winter. Ph.D. dissertation, The Florida State University, 177 pp. [Available from The Florida State University, Tallahassee, FL 32306.]

——, and Y. Hsueh, 1997: Inverse determination of surface heat flux over the Yellow Sea in 1986 winter from sea surface temperature data. *J. Phys. Oceanogr.,* in press.

Unauthenticated | Downloaded 09/28/22 11:35 PM UTC